Available online at www.sciencedirect.com
ScienceDirect
International Journal of Heat and Mass Transfer 50 (2007) 4409–4423
International Journal of HEAT and MASS TRANSFER
www.elsevier.com/locate/ijhmt

A regularization method for the inverse design of solidification processes with natural convection

K. Okamoto *, B.Q. Li

School of Mechanical and Materials Engineering, Washington State University, Pullman, WA 99164, United States

Received 23 January 2006; received in revised form 19 October 2006
Available online 10 May 2007

Abstract

An inverse algorithm is developed for the design of the solidification processing systems. The algorithm entails the use of the Tikhonov regularization method, along with the L-curve method to select an optimal regularization parameter. Both the direct solution of moving boundary problems and the inverse design formulation are presented. The design algorithm is applied to determine the optimal boundary heat flux distribution to obtain a unidirectional solid–liquid interface in a 2-D cavity. The inverse calculation is also performed with a prescribed sinuous solid–liquid interface. To this end, a whole time-domain method and a sequential method are used and evaluated. The L-curve based regularization method is found to be reasonably accurate for the purpose of designing solidification processing systems. We also found that the sequential method with appropriately selected time domains is comparative to the whole time-domain method.

Keywords: Inverse problems; The regularization method; L-curve; Solidification processes; Solid–liquid interface; The sequential method; The whole time-domain method

1. Introduction

Knowledge of liquid–solid interface morphology during solidification processing is of paramount importance to the microstructure formation in solidified materials. Because often the solid–liquid interface position is unknown *a priori*, the problem of finding the interface is classified as moving boundary problems. The widespread use of solidification principle in materials processing systems has resulted in both theoretical and experimental studies on the subject. A wide variety of numerical models have been developed for virtually every kind of solidification processing systems. Both the fixed grid and moving grid methods have been used to model the solidification phenomena. The former involves the use of enthalpy-based formulation in which the latent heat is factored into an effective heat capacity. The latter, however, tracks the solidification front, that is, the solid–liquid interface continuously by deforming the grids or elements. There are alternatives that involve a level set field variable to mark the solid–liquid interface. Model developed using these techniques have been applied mainly to answer the question concerning the interface position and morphological development for given operating conditions and specified geometric constraints.

In designing solidification processing systems, questions are often posed inversely. In practice a desired solidification microstructure in the final products dictates a certain type of solid–liquid interface front morphology. Thus question often arises of how the boundary heat flux distribution needs to be specified in order to obtain the desired solid–liquid interface during solidification processing. The objective of this paper is to present a numerical algorithm for the purpose of inversely designing solidification processing systems.

* Corresponding author. Present address: 2830-5 Yukinaga, Maizuru-shi Kyoto 625-0052, Japan.
E-mail address: keio13@wsu.edu (K. Okamoto).

0017-9310/$ - see front matter © 2007 Elsevier Ltd. All rights reserved.
doi:10.1016/j.ijheatmasstransfer.2006.10.019

Nomenclature

Mathematical symbol

$\|\ \|$	norm of a matrix or vector

Latin symbols

$\mathbf{A}$	coefficient matrix
$\mathbf{B}_T$	coefficient matrix
C	specific heat
$\mathbf{D}_T$	coefficient matrix
$\mathbf{d}$	solidification interface distance
$\bar{\mathbf{d}}$	ideal solidification interface distance
$\mathbf{E}$	coefficient matrix
$\mathbf{F}$	coefficient matrix
f	trial function
$\mathbf{G}_T$	coefficient matrix
$\mathbf{g}$	gravity force
H	latent heat
$\hat{i}$, $\hat{j}$	unit vectors of ith, jth components
I	number of piecewise functions
J	sensitivity coefficient matrix
$\mathbf{K}$	coefficient matrix
k	thermal conductivity
$\mathbf{L}_T$	coefficient matrix
L	number of controlled parameters for time
$\mathbf{M}$	coefficient matrix
$\mathbf{M}_p$	coefficient matrix
M	number of controlled parameters for space
$\mathbf{N}_T$	coefficient matrix
N	number of unknowns
$\mathbf{n}$	normal direction
P	piecewise function
p	pressure
$\mathbf{q}$	heat flux
S	sum of squares error
T	temperature
s	solid–liquid interface
T_m	melting temperature
t	time
$\mathbf{u}$	velocity
V	volume
x, y	coordinates

Greek symbols

α	regularization parameter
β	thermal expansion coefficient
ε	penalty parameter for pressure
Φ	monotonically increasing function
ϕ	shape function for velocity
λ	perturbation value
μ	viscosity
θ	shape function for temperature
ρ	density
σ	standard deviation
τ	viscous stress tensor
Ω	computational domain
ψ	shape function for pressure

Subscripts

i, j	i, jth points
m	melting
max	maximum value
l	liquid
s	solid

Superscripts

T	transpose
K	iteration number

Inverse heat transfer problems are well known in heat transfer community. Several monographs have also been devoted to the subject. It is a well-known fact that the inverse heat transfer problem is ill posed generally, although physically possible. Thus, solution of the inverse heat transfer problems often requires some sorts of regularization to make the problem solvable. The authors [1] have recently developed and evaluated several inverse algorithms in the heat conduction problem: the regularization method, the singular value decomposition (SVD), and the Levenberg–Marquardt method.

It is, however, conceivable that inverse free boundary problems can be more complex in general than inverse heat conduction problems. One of the applications of the inverse problems for solidification processing systems is the determination of the boundary condition by utilizing either experimental measurements (inverse solidification problems) or prescribed conditions (optimal solidification design problems). The inverse solidification problems have been investigated in literature. Krishnan and Sharma [2] found casting/mold interfacial heat transfer coefficients using experimental temperature measurements for casting solidification problems. They used the finite difference method (FDM) combined with the Beck's method for their inverse algorithm. O'Mahoney and Browne [3] combined their inverse algorithm with the integral-derivative method to find interfacial heat transfer coefficients using temperature measurements. Xu and Naterer [4] found temperature distribution using the prescribed solid–liquid interface location and heat fluxes. Hale et al. [5] used the Global Time Method (GTM) for their inverse algorithm to find heat flux distribution in the boundary of both liquid and solid phase using the prescribed temperature and heat flux in the liquid–solid interface. In their approach, the solid and liquid regions are treated as two distinct inverse heat transfer problems. Dulikravich et al. [6] found optimal

magnetic fields on the boundary by specifying desired magnetic field lines and temperature distribution. Zabaras et al. [7–11] studied the inverse solidification problems both with and without fluid flow being considered. They reported various algorithms including the Beck's method, the steepest descent method (SDM), and the conjugate gradient method (CGM). The authors [12] recently applied the regularization method for the inverse steady-state solidification problem to find the optimal heat flux distribution for the prescribed solid–liquid interface. Most of the work up to date has been limited to conduction mode only and few have considered the fluid flow effects. In addition, the prescribed solid–liquid interfaces in the previous work have been limited to the simple shapes such as a straight line.

In this paper, we present an inverse computational methodology for the solution of designing solidification processes. The motivation for this work is derived from the successful study in the heat transfer community for the prediction of heat transfer coefficients and thermophysical properties using measured thermal data such as temperature distribution and reported work on the subject. Unlike the previously reported study on the inverse solidification problems, our algorithm is based on the Tikhonov regularization method, along with carefully selected regularization parameter. The formulation of the problem and selection of the regularization parameter for moving boundary problems are discussed, along with the L-curve method to select an optimal regularization parameter for the inverse design calculations. The design algorithm is applied to determine the optimal boundary heat flux distribution to obtain unidirectional and sinuous solid–liquid interfaces in a 2-D cavity. To this end, we use parameter estimation analysis with a whole time-domain method and a sequential method.

2. The direct versus inverse solidification problem

2.1. Direct solidification problems

Fig. 1 schematically illustrates the 2-D model for the solidification problem under consideration. The top and bottom walls are thermally insulated. The temperature on the left wall is fixed at a constant temperature above the melting point, while the right hand-side wall is subject to cooling. The melt, which is initially above the melting temperature, starts to solidify as a result of cooling at the right-side wall. The fluid flow and heat transfer in the system are governed by the continuity equation, the Navier–Stokes equations, and the energy balance equation. For the melt flow, the standard Boussinesq approximation, $\rho = \rho_0[1 - \beta(T - T_m)]$, has been used. The governing equations for the problem are given as follows:

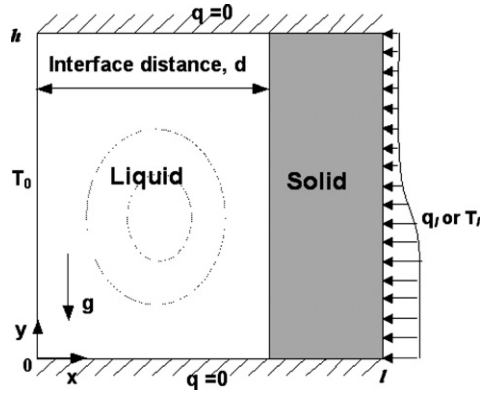

Fig. 1. Schematic of a solidification process in a 2-D cavity.

In the liquid region

$$\nabla \cdot \mathbf{u} = 0 \tag{1}$$

$$\rho \frac{\partial \mathbf{u}}{\partial t} + \rho \mathbf{u} \cdot \nabla \mathbf{u} = -\nabla p + \mu \nabla^2 \mathbf{u} - \mathbf{g}\rho_0 \beta (T - T_m) \tag{2}$$

$$\rho C \frac{\partial T}{\partial t} + \rho C \mathbf{u} \cdot \nabla T = k \nabla^2 T \tag{3}$$

In the solid region

$$\rho C \frac{\partial T}{\partial t} = k \nabla^2 T \tag{4}$$

On the solid–liquid interface

$$n \cdot k \nabla T|_l - n \cdot k \nabla T|_s = \rho H \frac{\partial s}{\partial t} \tag{5}$$

In the above equations, $\mathbf{u}$ is velocity, T the temperature, ρ the density, μ the viscosity, k the thermal conductivity, β the thermal expansion coefficient, T_m the melting temperature, p the pressure, C the specific heat, $\mathbf{g}$ the gravity, H the latent heat, and s the solid–liquid interface. The no slip condition is specified at the walls. The boundary conditions are as follows:

$$\mathbf{u} = 0 \quad \text{at all boundaries} \tag{6}$$

$$\frac{\partial T}{\partial y} = 0 \quad \text{at } y = 0 \text{ and } y = h \tag{7}$$

$$T = T_o \quad T_o > T_m \quad \text{at } x = 0 \tag{8}$$

$$T = T_L \quad \text{or} \quad q = q_L T_m > T_L \quad \text{at } x = l \tag{9}$$

where q is the heat flux. The solid–liquid interface is to be obtained for the direct problem or the well-posed problem. For the inverse problem, however, the solid–liquid interface shape is specified, and the cooling condition on the right wall is to be obtained.

2.2. Solution of direct problems

The governing equations described above along with the boundary conditions are solved using the deforming Galerkin finite element method. The stiffness matrix is obtained by using Galerkin's method of Weighted Residuals. The formulations and relevant benchmark tests were detailed in a series of papers published earlier [13–16] and thus only a brief summary is given here. The computational domain is first divided into small elements. With each element, the

dependent variable **u**, P and T are interpolated by shape functions ϕ, ψ and θ.

$$\mathbf{u}_i(x,t) = \phi^{\mathrm{T}}\mathbf{U}_i(t) \tag{10}$$

$$P(x,t) = \psi^{\mathrm{T}}\mathbf{P}(t) \tag{11}$$

$$T(x,t) = \theta^{\mathrm{T}}\mathbf{T}(t) \tag{12}$$

where the **U**, **P** and **T** are column vectors of element nodal point unknowns. Substituting Eqs. (10)–(12) into the governing equations (1)–(3), we get the residuals $R1$, $R2$ and $R3$ between the real solutions and the finite element solutions of the continuity equation, momentum equations, and energy equations respectively. The Galerkin form of the Method of Weighted Residuals seeks to reduce these errors to zero, and the shape functions are chosen the same as the weighting function. The governing equations are recast in an integral form, and the field variables are interpolated using shape functions over the computational domain. With an appropriate algebraic manipulation, the following set of equations are obtained:

$$\left(\int_\Omega \psi\,\widehat{i}\cdot\nabla\phi^{\mathrm{T}}\,\mathrm{d}V\right)\mathbf{U}_i = -\varepsilon\left(\int_\Omega \psi\psi^{\mathrm{T}}\,\mathrm{d}V\right)\mathbf{P} \tag{13}$$

$$\begin{aligned}&\left(\int_\Omega \rho\phi\phi^{\mathrm{T}}\,\mathrm{d}V\right)\frac{\mathrm{d}\mathbf{U}_i}{\mathrm{d}t} + \left(\int_\Omega \phi\rho\mathbf{u}\cdot\nabla\phi^{\mathrm{T}}\,\mathrm{d}V\right)\mathbf{U}_i - \left(\int_\Omega \hat{i}\cdot\nabla\phi\psi^{\mathrm{T}}\,\mathrm{d}V\right)\mathbf{P}\\ &+\left(\int_\Omega \mu\nabla\phi\cdot\nabla\phi^{\mathrm{T}}\,\mathrm{d}V\right)\mathbf{U}_i + \left(\int_\Omega \mu(\hat{i}\cdot\nabla\phi)(\hat{j}\cdot\nabla\phi^{\mathrm{T}})\,\mathrm{d}V\right)\mathbf{U}_j\\ &+\left(\int_\Omega \phi\theta^{\mathrm{T}}\rho\beta g\,\mathrm{d}V\right)(\mathbf{T}-\mathbf{T}_{\mathrm{m}}) = \int_{\partial\Omega}\mathbf{n}\cdot\tau\cdot\hat{i}\phi\,\mathrm{d}S\end{aligned} \tag{14}$$

$$\begin{aligned}&\left(\int_\Omega \rho C\theta\theta^{\mathrm{T}}\,\mathrm{d}V\right)\frac{\mathrm{d}\mathbf{T}}{\mathrm{d}t} + \left(\int_\Omega \rho C\theta\mathbf{u}\cdot\nabla\theta^{\mathrm{T}}\,\mathrm{d}V\right)\mathbf{T} + \left(\int_\Omega k\nabla\theta\cdot\nabla\theta^{\mathrm{T}}\,\mathrm{d}V\right)\mathbf{T}\\ &= -\int_{\partial\Omega} q_T\theta\,\mathrm{d}S\end{aligned} \tag{15}$$

where τ ($\tau_{ij} = \mu(u_{i,j} + u_{j,i})$) is the viscous stress tensor. Once the form of shape functions ϕ, ψ, and θ for velocity, pressure and temperature respectively are specified, the integrals defined in the above equations can be expressed in matrix form. Combining the momentum and energy equations into a single matrix equation gives rise to the following element stiffness matrix equation:

$$\begin{bmatrix}\mathbf{M} & 0\\ 0 & \mathbf{N}_T\end{bmatrix}\begin{bmatrix}\dot{\mathbf{U}}\\ \dot{\mathbf{T}}\end{bmatrix} + \begin{bmatrix}\mathbf{A}(\mathbf{U})+\mathbf{K}+\frac{1}{\varepsilon}\mathbf{E}\mathbf{M}_p^{-1}\mathbf{E}^{\mathrm{T}} & \mathbf{B}_T\\ 0 & \mathbf{D}_T(\mathbf{U})+\mathbf{L}_T\end{bmatrix}\begin{bmatrix}\mathbf{U}\\ \mathbf{T}\end{bmatrix} = \begin{bmatrix}\mathbf{F}\\ \mathbf{G}_T\end{bmatrix} \tag{16}$$

Note that in constructing the above element matrix equation, the penalty formulation has been applied, and **P** in the momentum equation is substituted by $\frac{1}{\varepsilon}\mathbf{M}_p^{-1}\mathbf{E}^{\mathrm{T}}\mathbf{U}$. The assembled global matrix equations are stored in the skyline form and solved using the Gaussian elimination method. The coefficient matrices of Eq. (16) above are calculated by

$$\mathbf{M}_p = \int_\Omega \psi\psi^{\mathrm{T}}\,\mathrm{d}V,\quad \mathbf{N}_T = \int_\Omega \rho C\theta\theta^{\mathrm{T}}\,\mathrm{d}V,\quad \mathbf{M} = \int_\Omega \rho\phi\phi^{\mathrm{T}}\,\mathrm{d}V,$$

$$\mathbf{E}_i = \int_\Omega \widehat{i}\cdot\nabla\phi\psi^{\mathrm{T}}\,\mathrm{d}V$$

$$\mathbf{L}_T = \int_\Omega k\nabla\theta\cdot\nabla\theta^{\mathrm{T}}\,\mathrm{d}V,\quad \mathbf{A}(\mathbf{U}) = \int_\Omega \rho\phi\mathbf{u}\cdot\nabla\theta^{\mathrm{T}}\,\mathrm{d}V,$$

$$\mathbf{D}_T(\mathbf{U}) = \int_\Omega \rho C\theta\mathbf{u}\cdot\nabla\theta^{\mathrm{T}}\,\mathrm{d}V$$

$$\mathbf{B}_T = \int_\Omega \rho\beta\mathbf{g}\phi\theta^{\mathrm{T}}\,\mathrm{d}V,\quad \mathbf{G}_T = -\int_{\partial\Omega} q_T\theta\,\mathrm{d}S,$$

$$\mathbf{F} = \int_{\partial\Omega} n\cdot\tau\phi\,\mathrm{d}S + \int_\Omega \rho\beta g\phi\theta^{\mathrm{T}}T_{\mathrm{m}}\,\mathrm{d}V$$

$$\mathbf{K}_{ij} = \left(\int_\Omega \mu\nabla\phi\cdot\nabla\phi^{\mathrm{T}}\,\mathrm{d}V\right)\delta_{ij} + \int_\Omega \mu(\hat{i}\cdot\nabla\phi)\left(\hat{j}\cdot\nabla\phi^{\mathrm{T}}\right)\mathrm{d}V$$

To implement the deforming finite elements to model the dynamic change of the moving interface, i.e., solidification front between the liquid and solid, a quasi-Lagrangian description is adopted. By this method, a region that covers the solidifying liquid and solid is defined and the nodes within the region are allowed to move in accordance with the interface movement. These additional velocities that result from the mesh movement are added to the velocity field as given in the above equations. The energy balance equation describing the latent heat release and interface change is directly integrated within the context of weighted residuals

$$\begin{aligned}&\left(\int_\Omega k\theta\hat{n}\cdot\nabla\theta^{\mathrm{T}}\,\mathrm{d}V\right)\mathbf{T}_{\mathrm{l}} - \left(\int_\Omega k\theta\hat{n}\cdot\nabla\theta^{\mathrm{T}}\,\mathrm{d}V\right)\mathbf{T}_{\mathrm{s}}\\ &= -\int_{\partial\Omega}\rho H\frac{\partial s}{\partial t}\theta\,\mathrm{d}S\end{aligned} \tag{17}$$

which is applied as a surface energy source to the total thermal energy balance equation, and added to the right-hand side of Eq. (16). The above equation systems are solved iteratively. Separation of the moving interface boundary coordinates from the global finite element solutions for field variables, however, requires the convergence of both moving interface coordinates and field variables in two related loops. The interface tracking strategy used in the present study involves an iterative procedure that entails applying the energy balance equation along with the interface as a surface source and searching for the interface position coordinates based on each converged field calculations. The updated interface positions are then fed back to the field calculations until both the interface position coordinates and field variables are converged within a preset criterion, which is set at 1×10^{-4} (relative error) for the results presented below.

2.3. Solution of inverse solidification problems

The inverse solidification problem seeks the heat flux distribution **q** that leads to a given solid–liquid interface distance $\bar{\mathbf{d}}$. Note that solidification interface distance, **d**, is

defined as the length between the left wall and the solid–liquid interface (Fig. 1). For the purpose of a numerical analysis, we consider the unknown function $\mathbf{q}$ to be parameterized in the following form:

$$\mathbf{q} = \sum_{j=1}^{N} q_j f_j(y,t) \tag{18}$$

where $f_j(y,t)$ $(j = 1,\ldots,N)$ are known trial functions. This approach is categorized to the parameter estimation approach. The inverse solution is to estimate the N unknown parameters q_j $(j = 1,\ldots,N)$ by minimizing the following objective function for the zeroth-order regularization method

$$S(\mathbf{q}) = \sum_{i=1}^{L}\sum_{j=1}^{M}\left[\bar{d}_{ij} - d_{ij}(\mathbf{q})\right]^2 + \alpha\sum_{i=1}^{N} q_i^2 \tag{19}$$

where q_i is the unknown parameters, $\bar{d}_{ij}$ is the ideal solidification interface distance for time and space, $d_{ij}(\mathbf{q})$ is the estimated solidification interface distance corresponding to the same time and space as $\bar{d}_{ij}$, L is the number of controlled solidification distance for time, M is the number of controlled solidification distance for space, and N is the total number of unknown parameters. Note that in this study the zeroth-order regularization method is more appropriate than the first- or second-order regularization method because reducing the magnitudes of the parameters are more important than reducing the changes of the parameters or the second differences of the parameters. In the above equation, α is the regularization parameter. Eq. (19) can be written in matrix form

$$S(\mathbf{q}) = \left[\bar{\mathbf{d}} - \mathbf{d}(\mathbf{q})\right]^{\mathrm{T}}\left[\bar{\mathbf{d}} - \mathbf{d}(\mathbf{q})\right] + \alpha\mathbf{q}^{\mathrm{T}}\mathbf{q} \tag{20}$$

where $\mathbf{q}^{\mathrm{T}}=[q_1, q_2, \ldots, q_i, \ldots, q_N]$, $\bar{\mathbf{d}} = \left[\bar{\mathbf{d}}_1\bar{\mathbf{d}}_2\cdots\bar{\mathbf{d}}_i\cdots\bar{\mathbf{d}}_L\right]^{\mathrm{T}} = [\bar{d}_{11}\bar{d}_{12}\cdots\bar{d}_{1n}\bar{d}_{21}\cdots\bar{d}_{ij}\cdots\bar{d}_{LM}]^{\mathrm{T}}$, $\mathbf{d}(\mathbf{q}) = [\mathbf{d}_1\mathbf{d}_2\cdots\mathbf{d}_L]^{\mathrm{T}} = [d_{11}d_{12}\cdots d_{1M}d_{21}\cdots d_{LM}]^{\mathrm{T}}$. To minimize the least squares norm given by Eq. (20), the derivatives of $S(\mathbf{q})$ with respect to each of the unknown parameters $[q_1, q_2, \ldots, q_N]$ are set to zero, that is

$$\frac{\partial S(\mathbf{q})}{\partial q_1} = \frac{\partial S(\mathbf{q})}{\partial q_2} = \cdots = \frac{\partial S(\mathbf{q})}{\partial q_N} = 0 \tag{21}$$

This necessary condition for the minimization of $S(\mathbf{q})$ can be expressed in matrix notation by equating the gradient of $S(\mathbf{q})$ to zero, that is

$$\nabla S(\mathbf{q}) = 2\left[-\frac{\partial \mathbf{d}^{\mathrm{T}}(\mathbf{q})}{\partial \mathbf{q}}\right]\left[\bar{\mathbf{d}} - \mathbf{d}(\mathbf{q})\right] + 2\alpha\mathbf{q}^{\mathrm{T}} = 0 \tag{22}$$

Defining a sensitivity coefficient matrix

$$\mathbf{J}(\mathbf{q}) = \left[\frac{\partial \mathbf{d}^{\mathrm{T}}(\mathbf{q})}{\partial \mathbf{q}}\right]^{\mathrm{T}} \tag{23}$$

If a forward difference scheme is used, the sensitivity coefficient matrix with respect to q_j is approximated by

$$J_{ij} \cong \frac{d_i(q_1, q_2, \ldots, q_j + \lambda q_j, \ldots, q_N) - d_i(q_1, q_2, \ldots, q_j, \ldots, q_N)}{\lambda q_j} \tag{24}$$

where $\lambda \approx 10^{-3}$. Eq. (22) becomes

$$\mathbf{J}^{\mathrm{T}}(\mathbf{q})\left[\bar{\mathbf{d}} - \mathbf{d}(\mathbf{q})\right] = \alpha\mathbf{q} \tag{25}$$

For the non-linear problems, when the sensitivity coefficient has some functional dependence on the vector of unknown parameters $\mathbf{q}$, the problem is referred to as the non-linear inverse problem. By the Taylor series expansion

$$\mathbf{d}(\mathbf{q}^{K+1}) = \mathbf{d}(\mathbf{q}^{K}) + \mathbf{J}(\mathbf{q}^{K})(\mathbf{q}^{K+1} - \mathbf{q}^{K}) \tag{26}$$

where K is an iteration index. Eq. (25) becomes

$$\mathbf{J}^{\mathrm{T}}(\mathbf{q}^{K+1})\left[\bar{\mathbf{d}} - \mathbf{d}(\mathbf{q}^{K+1})\right] = \alpha\mathbf{q}^{K+1} \tag{27}$$

Using Eq. (26) for the non-linear equation, Eq. (27) becomes

$$\mathbf{J}^{\mathrm{T}}(\mathbf{q}^{K+1})\left[\bar{\mathbf{d}} - \mathbf{d}(\mathbf{q}^{K}) - \mathbf{J}(\mathbf{q}^{K})(\mathbf{q}^{K+1} - \mathbf{q}^{K})\right] = \alpha\mathbf{q}^{K+1} \tag{28}$$

and then

$$\mathbf{q}^{K+1} = \left[(\mathbf{J}(\mathbf{q}^{K+1}))^{\mathrm{T}}\mathbf{J}(\mathbf{q}^{K}) + \alpha\mathbf{I}\right]^{-1}(\mathbf{J}(\mathbf{q}^{K+1}))^{\mathrm{T}}\left[\bar{\mathbf{d}} - \mathbf{d}(\mathbf{q}^{K}) + \mathbf{J}(\mathbf{q}^{K})^{\mathrm{T}}\mathbf{q}^{K}\right] \tag{29}$$

Further assuming $\mathbf{J}(\mathbf{q}^{K+1}) \approx J(\mathbf{q}^{K})$, we have the following estimate for the unknown heat flux distribution:

$$\mathbf{q}^{K+1} = \left[(\mathbf{J}(\mathbf{q}^{K}))^{\mathrm{T}}\mathbf{J}(\mathbf{q}^{K}) + \alpha\mathbf{I}\right]^{-1}(\mathbf{J}(\mathbf{q}^{K}))^{\mathrm{T}}\left[\bar{\mathbf{d}} - \mathbf{d}(\mathbf{q}^{K}) + \mathbf{J}(\mathbf{q}^{K})^{\mathrm{T}}\mathbf{q}^{K}\right] \tag{30}$$

2.4. The L-curve method

It is well known that the success of the regularized minimization method described above depends on an appropriate choice of the regularization parameter. While many techniques may be used for this purpose, the L-curve appears to be useful for selecting the regularization parameter for moving boundary problems, because of the highly non-linear nature of the problems. Note that since the problem is non-linear, the Ordinary Cross-Validation (OCV), the Generalized Cross-Validation (GCV) and Maximum likelihood method (ML) methods, which were utilized in the inverse heat conduction problems [1], are in general ineffective to find the optimal regularization parameter. In addition, the discrepancy principle based on the measurement error is not utilized because error may not be easily specified. The L-curve method is considered a viable choice for this purpose. The L-curve method [17], which was first proposed by Hansen, is based on an algorithm that locates the 'corner' of a plot of the function of norm of computed heat fluxes, $\|\mathbf{q}\|$, versus norm of the difference between computed solidification distance and prescribed solidification distance, $\|\bar{\mathbf{d}} - \mathbf{d}\|$ (Fig. 2). Note that the norm $\|\cdot\|$ is defined by

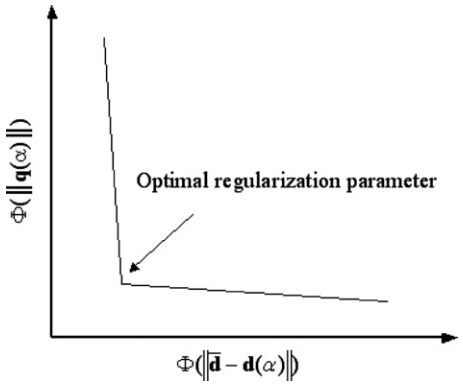

Fig. 2. Illustration of determining optimal α using the L-curve method. The corner point should be an optimal parameter.

$$\|\mathbf{q}\| = \left(\sum_{i=1}^{N} q_i^2\right)^{1/2} \tag{31}$$

Let Φ be a monotonically increasing function, we may define the curve

$$L = \left\{\Phi(\|\mathbf{q}\|), \Phi(\|\bar{\mathbf{d}} - \mathbf{d}\|) : \alpha > 0\right\} \tag{32}$$

where Φ is chosen to be one of the following functions:

$$\Phi(t) = t, \quad \Phi(t) = \sqrt{t}, \quad \text{or } \Phi(t) = \frac{1}{2}\log_{10} t, \ \ t > 0 \tag{33}$$

In this way, we evaluate the compromised solution between the residual error $\|\bar{\mathbf{d}} - \mathbf{d}\|$ and the smoothness of the solution $\|\mathbf{q}\|$.

2.5. Sequential method and whole time-domain method

The time domain in which the inverse problem is calculated may be another way to classify the methods of solution. Several schemes have been proposed for the time-dependent inverse problem. A whole time-domain method and a sequential method are useful methods for a parameter specification inverse problem. The whole time-domain method utilizes the whole part of the time domain to compute unknown parameters in the inverse algorithm. On the other hand, the time domain in the sequential method is split into some parts of the time domain. Then unknown variables in each time domain are calculated separately and independently. The final conditions that are calculated in each time domain are carried over to the next time domain for the initial conditions. In the regularization method, the most of the computation time is spent for computing the sensitivity coefficient matrix (Eq. (23)). All of the time steps must be considered to form the sensitivity coefficient matrix for the whole time-domain method. Therefore, the whole time-domain method is computationally expensive and time-consuming. On the other hand, each time domain in the sequential method has the smaller number of the time steps than in the whole time-domain method. As a result, the number of the sensitivity coefficients to compute is reduced. Therefore, the sequential method allows us to store small space of a computer memory. In addition, the computation time of the sequential method is faster than that of the whole time-domain method. The whole time-domain method, however, may be suitable for the problems where variables in the early time domain affect the controlled parameters in the late time. These problems include the solidification process in which the effect of diffusion and latent heat is considered. We use and evaluate both the whole time-domain and sequential methods in this paper.

2.6. Scaling

We use a polynomial approximation for the trial functions (Eq. (18)) to find optimal heat flux solutions. When variables of the polynomial function are either in a small or large range, *scaling* needs to be performed for the variables of the polynomial functions. *Scaling* is a transformation of the polynomial function in order to obtain an optimal solution of the inverse calculations. The poorly scaled functions make the solution more unbalanced. For example, when a second order polynomial function, $q(y) = a_1 y^2 + a_2 y + a_3$ $(0 \leqslant y \leqslant 0.01)$, is used for approximating an optimal solution, the coefficient a_1 for y^2 has very small effect compared to a_2 and a_3 because y^2 is a very small value in $0 \leqslant y \leqslant 0.01$. In other words, $q(y)$ is less sensitive to small changes in a_1 than those in a_2. Thus, the sensitivity coefficients J_{i1} (Eq. (24)) for a_1 become very small. When these sensitivity coefficients are used to find the optimal solution, we obtain the solution in which the value of $a_1 y^2$ is small and negligible. That is, the solution using this polynomial function has a strong linear relationship between y and q. For overcoming this drawback, the polynomial function should be changed to

$$q(y) = a_1 \cdot (10^{-4} y^2) + a_2 \cdot (10^{-2} y) + a_3$$

Since the variables ($10^{-4}y^2$, $10^{-2}y$, and 1) are linearly independent and generate a second order polynomial function, no loss of generality is incurred by the use of the scaled polynomial function. In addition, the scaled function makes the solution more balanced. If the above polynomial function were used, the trial functions of Eq. (18) would be

$$f_1(y,t) = 10^{-4} y^2$$
$$f_2(y,t) = 10^{-2} y$$
$$f_3(y,t) = 1$$

2.7. Piecewise functions

In the whole time-domain method, we use the piecewise approximation for an optimal heat flux solution. The final time t_f is given in the calculation. We split the time domain into I domains as follows:

$$0 = t_0 < t_1 < t_2 < \cdots < t_I = t_f \tag{34}$$

Piecewise functions $P_i(t)$ are defined as

$$P_i(t), \quad t_{i-1} < t < t_i, \ \ i = 1, \ldots, I \tag{35}$$

If the above piecewise function were used for the inverse calculation, the parameterized function of Eq. (18) would be

$$q = P_i(t) = \sum_{j=1}^{N} q_j^i f_j^i(y,t), \quad t_{i-1} < t < t_i, \ \ i = 1, \ldots, I \tag{36}$$

Unknown parameters of $I \times N$ would be found in the inverse calculations.

3. Numerical implementation, results and discussion

The direct and inverse algorithms described above enable the prediction of solid–liquid interface for a set of given boundary conditions and of the heat flux distribution along the boundaries for a prescribed interface movement. An inverse design of solidification process with natural convection is solved to find the optimal heat flux solution for specified solid–liquid interfaces. The regularization method along with the L-curve method is implemented for the inverse design solidification problem.

In this section, we address the direct transient solidification problem with convection and briefly discuss the effects of convection on the solid–liquid interface (Section 3.2). Finally, we consider the inverse design of solidification processes (Section 3.3). In particular, the initial conditions of the transient solidification problem is obtained using the inverse steady-state solidification problem without convection (Section 3.1)

In the direct and inverse problems, we consider a solidification process for pure aluminum confined in a square mold ($0 \leqslant x \leqslant 0.02m$, $0 \leqslant y \leqslant 0.02m$). Quadrilateral linear elements, 22×44, are used in each solid region and liquid region (Fig. 3).

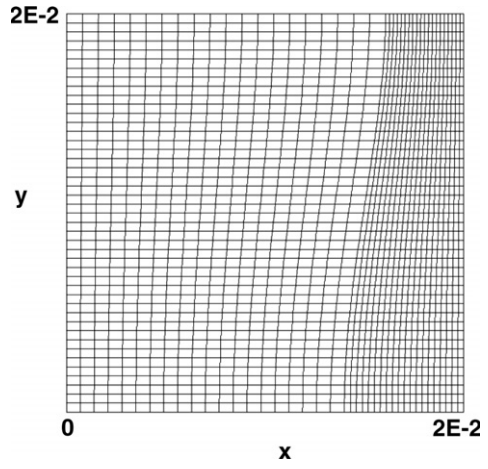

Fig. 3. Quadrilateral linear elements for the direct and inverse problems. The left side is specified as a liquid region. The right side is a solid region.

3.1. The inverse steady-state solidification problem without convection

First, the inverse steady-state solidification problem without natural convection is solved. The detail description for the inverse steady-state solidification problem is shown in [12]. The cavity is thermally insulated at the top and bottom. The left wall is fixed at $T = 1220$ K above the melting temperature ($T_m = 933$ K). The gravity force is not applied. The locations of the desired solid–liquid interface for the cases 1 and 2 are specified in Fig. 4. We find the optimal heat flux solution on the right wall required to achieve these solid–liquid interfaces. The direct problem is then solved to find the temperature distributions (Fig. 5a and b). These temperature distributions are used to set the initial conditions for the transient solidification calculations described below.

3.2. The direct problem for transient solidification processes with convection

The direct problems for transient solidification processes were studied extensively in [13–16]. Our objective to present the direct problem in this paper is to see how much a vertical straight line for the solid–liquid interface moves and deforms at a certain time by the effect of natural convection. The initial temperatures are given in Fig. 5a. Thus, the solid–liquid interface for the initial state is located at $x = 0.015$ vertically. The top and bottom walls are kept adiabatic. The temperature of the left wall is fixed at 1220 K, which is above the freezing temperature $T_m = 933$ K. The right side wall is imposed with heat extraction ($q = -4 \times 10^6$ W/m^2), which will cause the solidification to occur. The gravity force, 9.8 m/s^2, is applied downward.

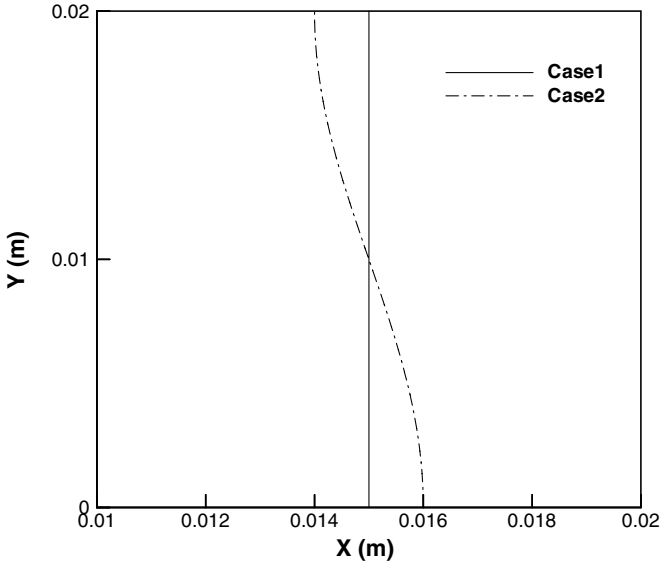

Fig. 4. Prescribed locations for the solid–liquid interface in the cases 1 and 2. Case 1 is a vertical straight line ($x = 0.015$). Case 2 is a sine curve ($x = -0.001\cos(50\pi(y - 0.02)) + 0.015$).

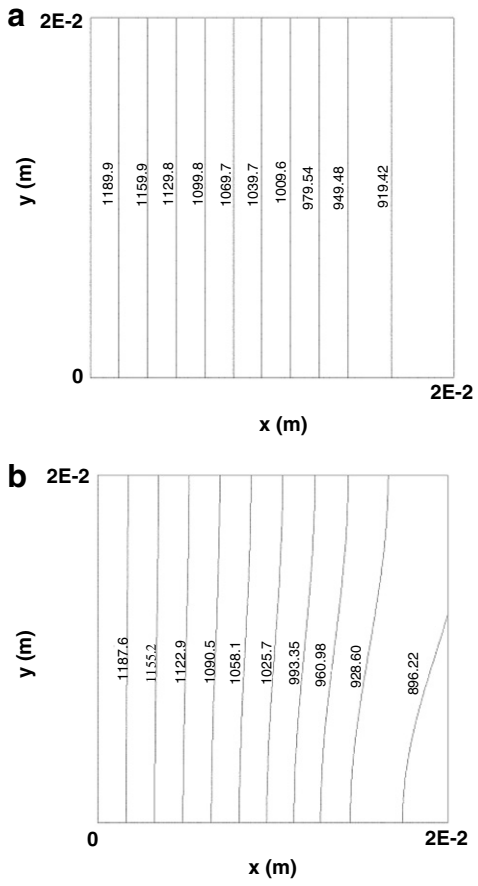

Fig. 5. Temperature distributions for the inverse steady-state solidification problem: (a) for the case 1, (b) for the case 2. These temperature distributions will be initial conditions for the transient calculations.

A constant time step $\Delta t = 0.02$ s is selected with the final time of 0.6 s. Fig. 6 shows the velocity distribution at $t = 0.6$ s. For this problem, it is found that the solid–liquid interface at $t = 0.6$ s is strongly affected by the convection in the cavity. If the natural convection were not present, a vertical solidification front would have been achieved. We also see that the solidification occurs, and the solid–liquid interface moves leftward.

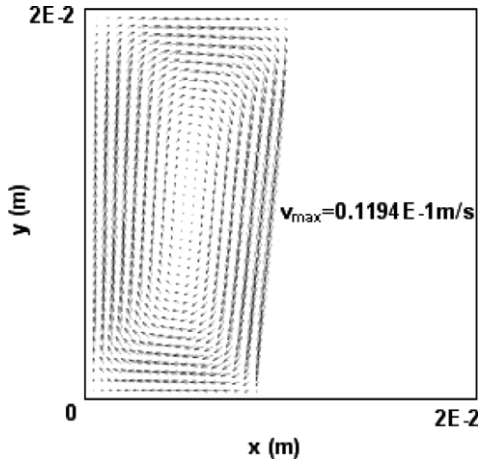

Fig. 6. Velocity distribution at $t = 0.6$ s for the direct solidification problem. The initial solid–liquid interface was located at $x = 0.015$ m vertically.

3.3. The inverse time-dependent solidification problem

We tested two cases for the inverse time-dependent solidification problems. In the case 1, the initial solid–liquid interface is a vertical straight line located at $x = 0.015$. The case 2 has an initial solid–liquid interface with a sine wave shown in Fig. 4. The initial temperatures in the cases 1 and 2 are given in Fig. 5a and b, respectively. The top and bottom walls are kept adiabatic. The temperature of the left wall is fixed at 1220 K. In addition to the above initial and boundary conditions, we also desire that solidification occur with the prescribed growth conditions where a desired solid–liquid interface is moving leftward with a prescribed constant velocity, 1.17×10^{-2} m/s. To this end, the ideal solidification distance $\bar{d}_{ij}$ is specified at every node point of the solid–liquid interface in every 0.04 seconds. Note that the interfacial velocity must be constant for a uniform microstructure in the final casting. The gravity force, 9.8 m/s^2, is applied downward. A constant time step $\Delta t = 0.02$ s is selected with the final time of 0.6 s. Our interest is to find the optimal heat flux distribution on the right wall in order to obtain prescribed solid–liquid interfaces. To evaluate the accuracy of our inverse algorithm, the standard deviation is defined in the following equation:

$$\sigma_i = \left(\frac{\sum_{j=1}^{M} \left(\bar{d}_{ij} - d_{ij} \right)^2}{M} \right)^{\frac{1}{2}} \tag{37}$$

where M is the number of controlled solidification distance for space. First, we use the parameter estimation with fourth order polynomial functions for time, t, and space, y. We also use the technique of scaling. Thus, the approximate heat flux solution is

$$q = q_1(10^8 y^4) + q_2(10^6 y^3) + q_3(10^4 y^2) + q_4(10^2 y) + q_5(10^4 t^4) + q_6(10^3 t^3) + q_7(10^2 t^2) + q_8(10t) + q_9 \tag{38}$$

The parameters q_1, q_2, q_3, q_4, q_5, q_6, q_7, q_8, q_9, are calculated in the regularization method with L-curve. If this inverse problem were solved in the function estimation (without using the polynomial approximation), the number of unknown parameters would be 1320 because there would be 44 unknown parameters for space and 30 unknown parameters for time. Thus, the parameter estimation with the polynomial function results in the significant reduction of the calculation time and the computer memory.

We first examine the convergence for the non-linear regularization method. Fig. 7 shows the convergence rate of the calculations. Two iterations are found to be enough for the regularization method to converge the calculations. Fig. 8 shows the L-curve plots for this problem. There is a convex point located at $\alpha = 1E{-}22$. Thus, we select 1E−22

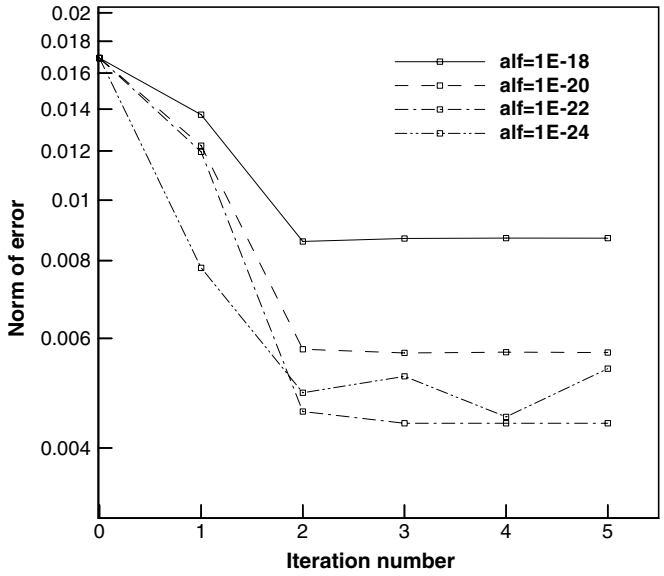

Fig. 7. Convergence rate for the whole time-domain method with nine unknowns in the case 1.

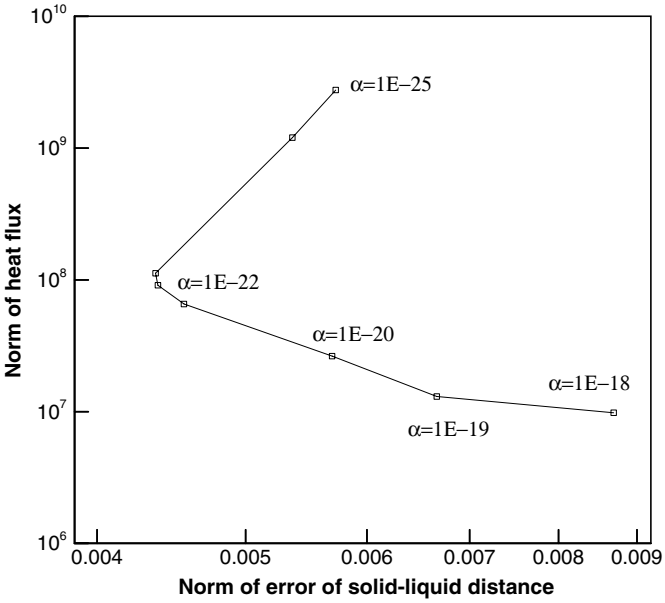

Fig. 8. L-curve method for the whole time-domain with nine unknowns. $\alpha = 1E{-}22$ is selected for the optimal regularization parameter.

as an optimal regularization parameter. Fig. 9 shows that the heat flux solution using $\alpha = 1E{-}22$. Fig. 10 is time history of the standard deviation σ Eq. (37) for the error of the solid–liquid interface by using the optimal heat flux solution. As seen from the figure, the error reaches the lowest point at $t = 0.28$ s and then shoots up until final time. Fig. 11 shows the percent errors of the solid–liquid distance at $t = 0.6$ s. The maximum percent error at $t = 0.6$ s is 5%. Since only nine unknown parameters for the polynomial functions are solved, the heat flux distribution (Fig. 9) found by the regularization method is a smooth and simple curve. To control the solidification distance accurately,

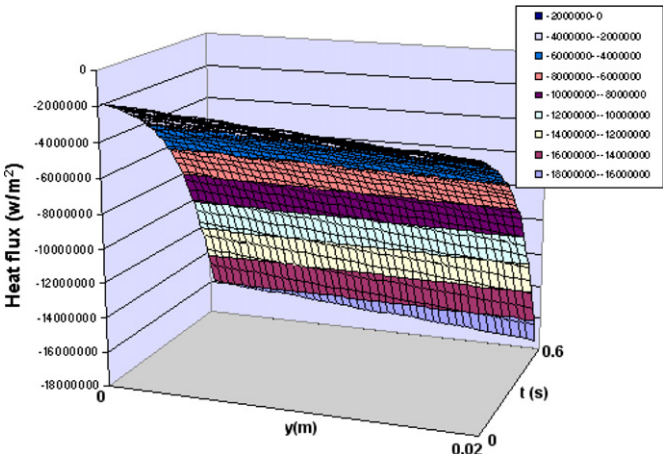

Fig. 9. Heat flux solution using the whole time-domain method with nine unknowns.

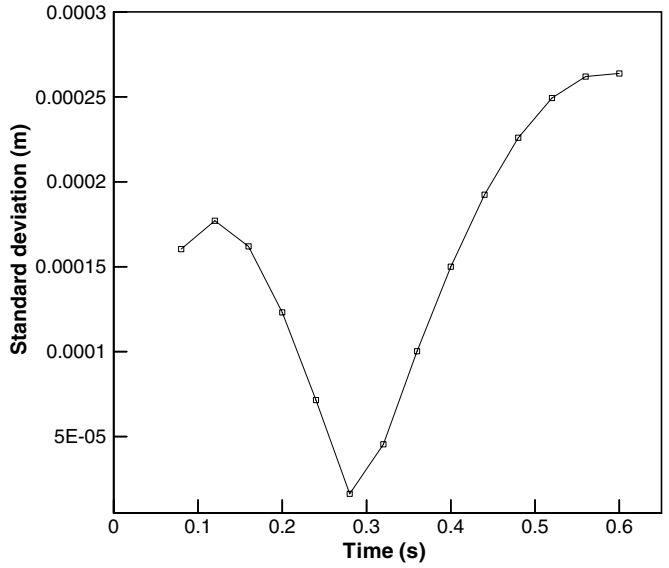

Fig. 10. Standard deviation for the whole time-domain method with nine unknowns.

more complex curve for the heat flux distribution needs to be obtained. For this purpose, we use the sequential method and the whole time-domain method with the piecewise polynomial functions. These two methods described below make the inverse calculations more accurate, but time-consuming.

3.3.1. Sequential method

In the sequential method, the time domain is split into some parts. Due to the diffusion time, it is critical to choose appropriate time domain in order to obtain the optimal heat flux solutions. After doing numerical experiments, we found that 0.2 s is enough time to calculate the optimal heat flux solution in this problem. Thus, we divide the time domain into three parts. The first time domain ranges from 0 s to 0.2 s followed by the second time domain ($0.2\text{ s} \leqslant t \leqslant 0.4$ s) and the third time domain

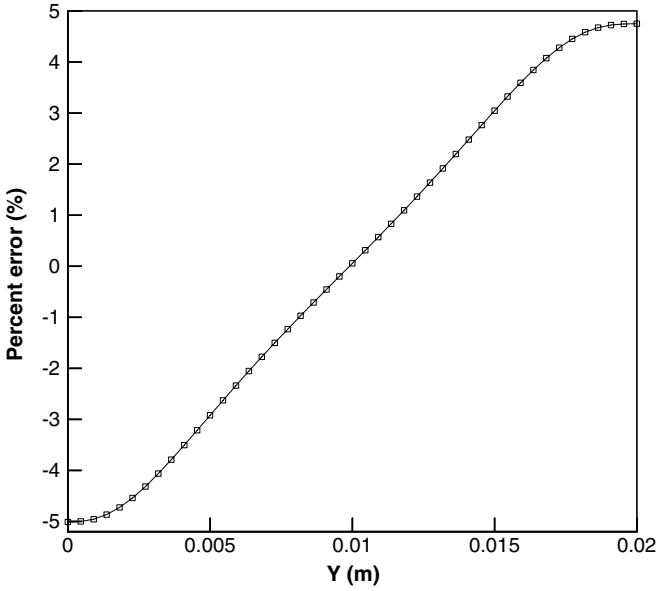

Fig. 11. Percent error of the solid–liquid distance at $t = 0.6$ for the whole time-domain method with nine unknowns.

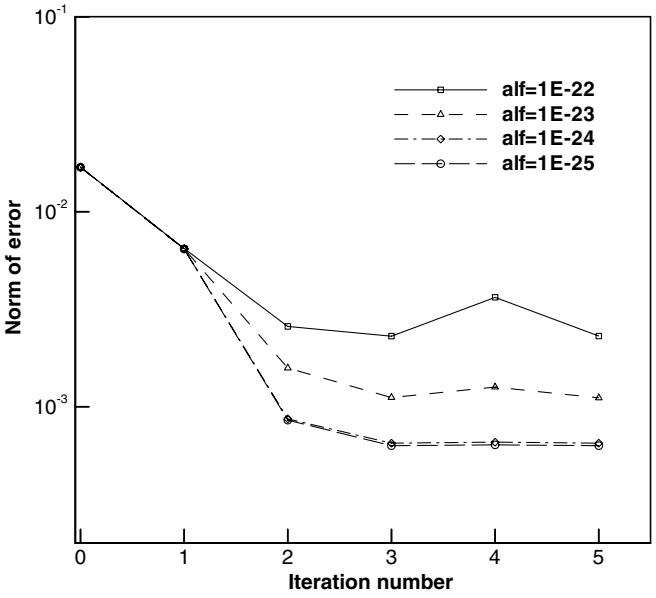

Fig. 13. Convergence rate for the case 1 for the whole time-domain method.

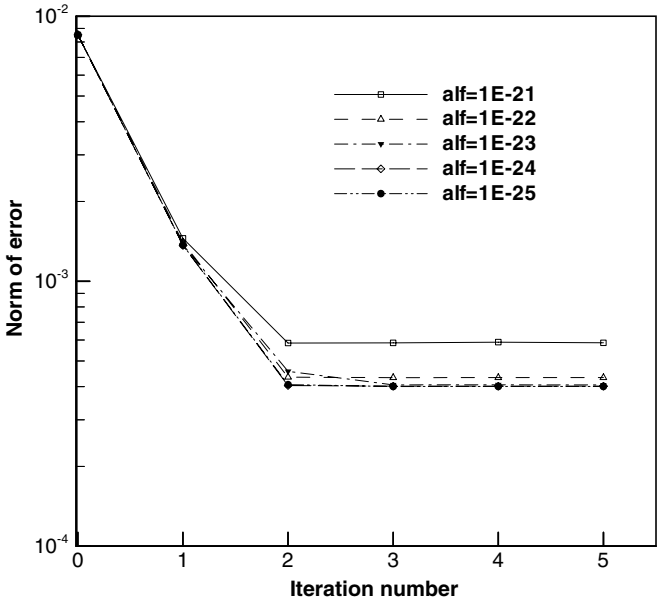

Fig. 12. Convergence rate for the first time domain in the case 1 for the sequential method.

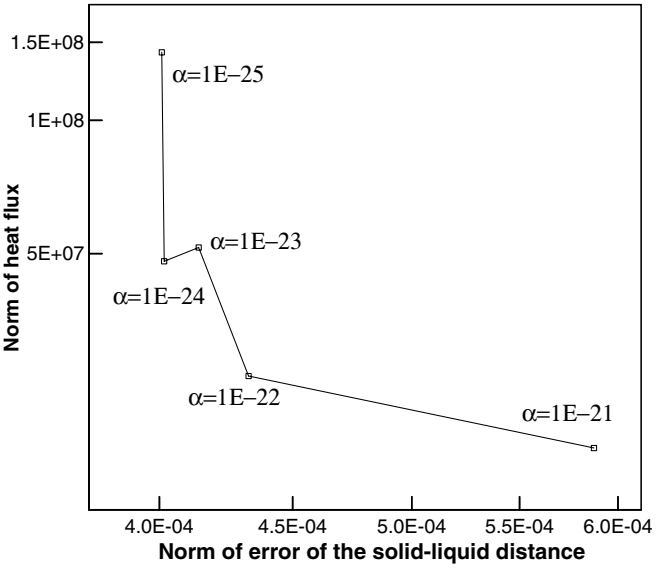

Fig. 14. L-curve method for the first time domain in the case 1 for the sequential method. The regularization parameter $\alpha = 1E{-}24$ is selected for the optimal solution.

(0.4 s $\leqslant t \leqslant$ 0.6 s). Each domain is calculated independently by using the regularization method. Thus, three calculations of the regularization methods are performed in a sequential manner. At the boundaries of the time domains ($t = 0.2$ s and 0.4 s), the temperature and velocity distributions are carried over to the next time domains. That is, the temperature and velocity distributions at $t = 0.2$ s calculated in the first time domain are used for the initial conditions in the second time domain. The same holds true for the conditions at $t = 0.4$ s for the second and third time domains. The following fifth order polynomial functions for time and space are used to find the optimal heat flux distribution:

$$q = q_1(10^8 y^4) + q_2(10^6 y^3) + q_3(10^4 y^2) + q_4(10^2 y) + q_5(10^4 t^4) + q_6(10^3 t^3) + q_7(10^2 t^2) + q_8(10t) + q_9 \quad (39)$$

where $0 \leqslant y \leqslant 0.02$, $0 \leqslant t \leqslant 0.2$. Nine unknown parameters, q_1, q_2, q_3, q_4, q_5, q_6, q_7, q_8, q_9, are computed in the inverse calculations for the each time domain. Thus, a total of 27 unknown parameters are solved in the sequential method.

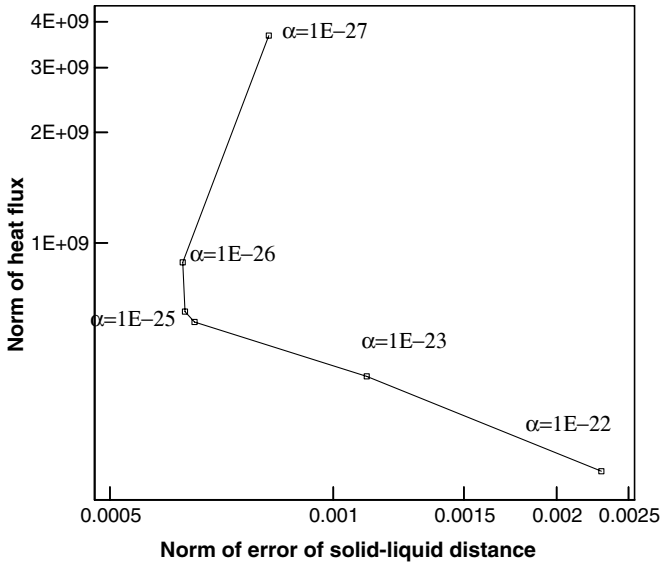

Fig. 15. L-curve method for the case 1 for the whole time-domain method. The regularization parameter $\alpha = 1E{-}25$ is selected for the optimal solution.

3.3.2. Whole time-domain method with piecewise polynomial functions

The piecewise polynomial functions are used to find the optimal heat flux solution. In the whole time-domain method, the following scaled piecewise polynomial functions are used:

$$\begin{aligned} q = {} & q_i(10^8 y^4) + q_{i+1}(10^6 y^3) + q_{i+2}(10^4 y^2) \\ & + q_{i+3}(10^2 y) + q_{i+4}\left[10^4 (t-a)^4\right] \\ & + q_{i+5}\left[10^3 (t-a)^3\right] + q_{i+6}\left[10^2 (t-a)^2\right] \\ & + q_{i+7}[10(t-a)] + q_{i+8} \end{aligned} \tag{40}$$

where

$$0 \leqslant y \leqslant 0.02, \quad \begin{cases} i = 1, a = 0 & \text{in } 0 \leqslant t \leqslant 0.2 \\ i = 10, a = 0.2 & \text{in } 0.2 \leqslant t \leqslant 0.4 \\ i = 19, a = 0.4 & \text{in } 0.4 \leqslant t \leqslant 0.6 \end{cases}$$

In the above equation, 27 coefficients of the polynomial function are solved by the regularization method. We use

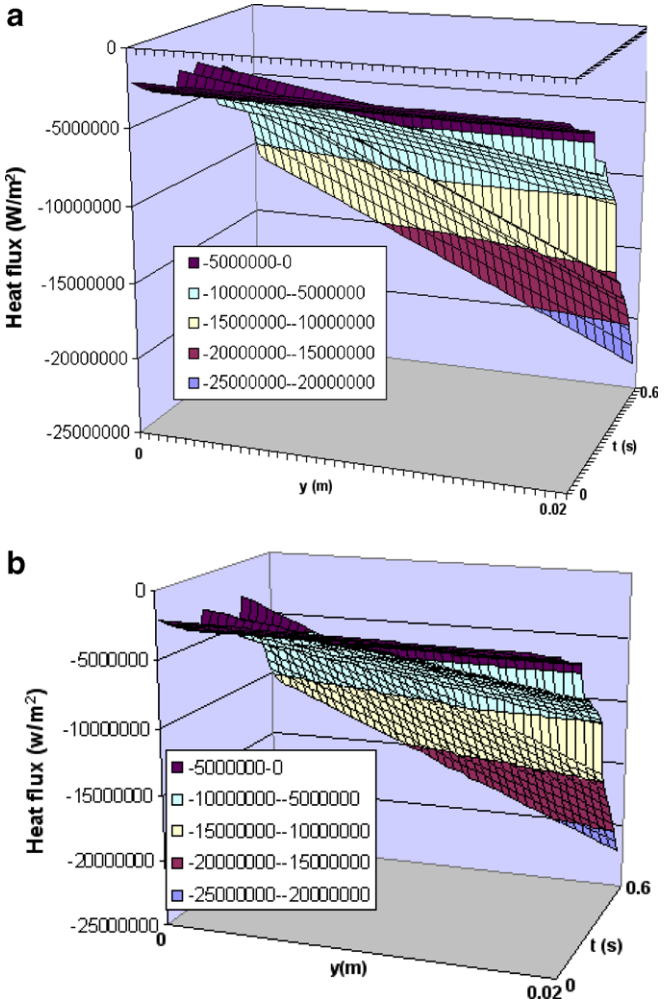

Fig. 16. Optimal heat flux solutions in the case 1 for (a) the sequential method and (b) the whole time-domain method with the piecewise polynomial function.

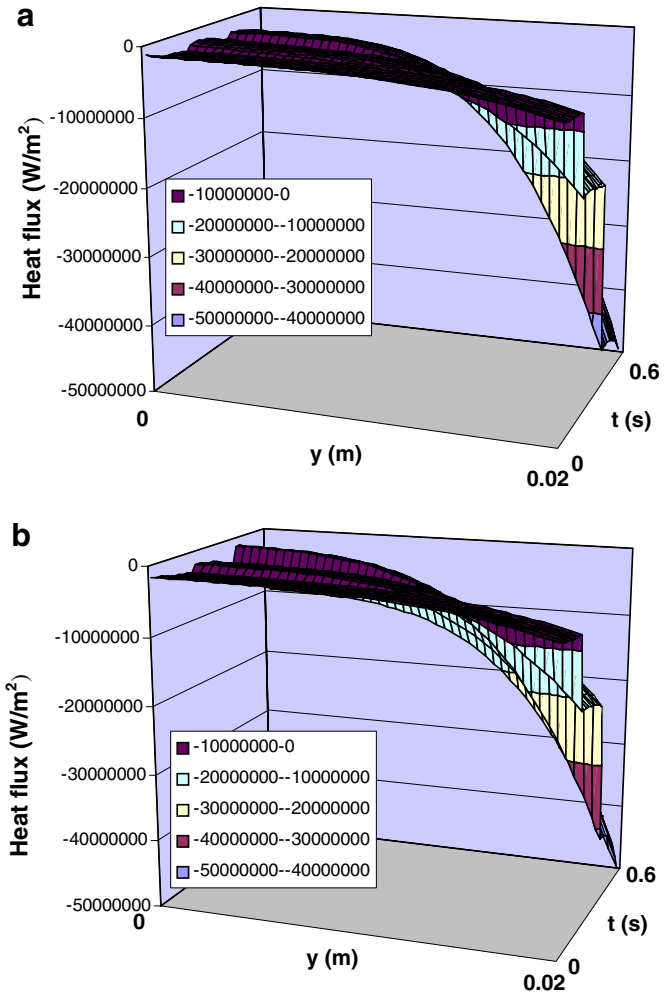

Fig. 17. Optimal heat flux solution in the case 2 for (a) the sequential method and (b) the whole time-domain method with the piecewise polynomial function.

the same-scaled function as in the sequential method using Eq. (39). Thus, when the whole time-domain method is compared to the sequential method, the difference of the scaling effect can be neglected.

3.3.3. Convergence rate

We first examine the convergence for the sequential method and the whole time-domain method. Figs. 12 and 13 show the convergence rate for the first time domain in case 1 for the sequential method and for the whole time-domain method with the piecewise polynomial function, respectively. In the sequential method, the convergence reaches at the second iteration. The whole time-domain method needs as little as three iterations for the convergence.

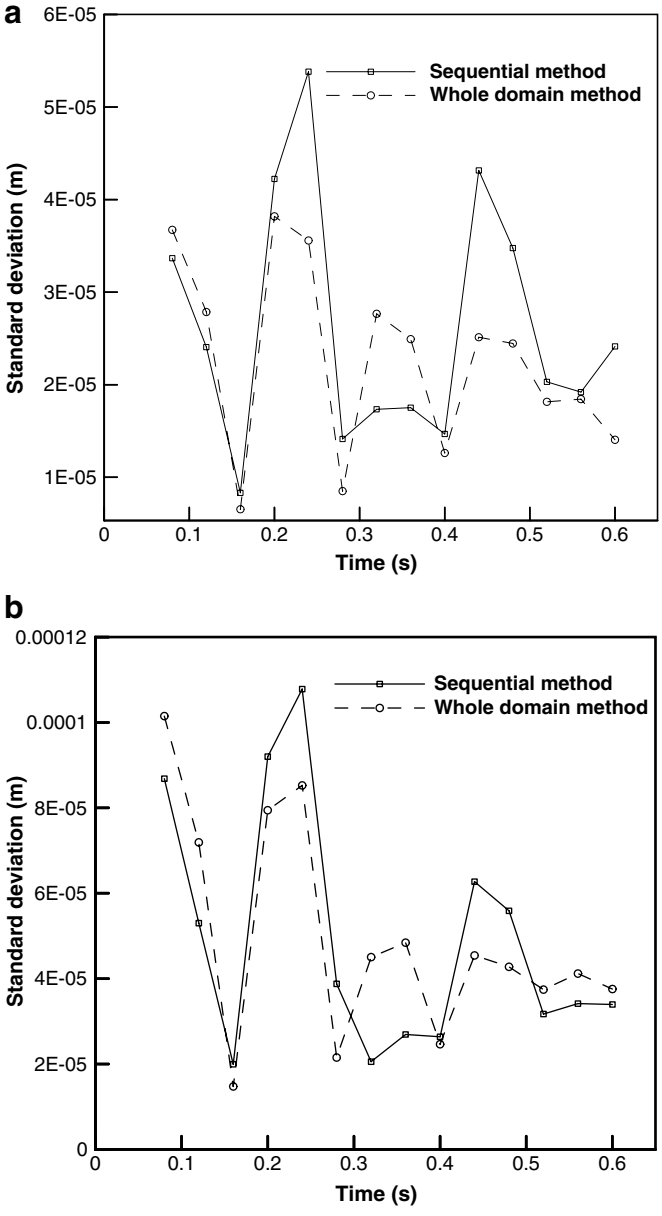

Fig. 18. Standard deviations σ (Eq. (37)) for the error of the solid–liquid distance for (a) the case 1 and (b) the case 2.

3.3.4. L-curve method

To find an optimal regularization parameter, the L-curve method is used for our calculation. Fig. 14 shows the L-curve plots for the first time domain of the sequential method in the case 1. Fig. 15 shows the L-curve plots for the whole time-domain method with the piecewise polynomial function in the case 1. These figures show the turning points, which are considered the optimal regularization parameters. The regularization parameters, $\alpha = 1E{-}24$ and $1E{-}25$, are selected in the sequential method and the whole time-domain method, respectively. For other cases,

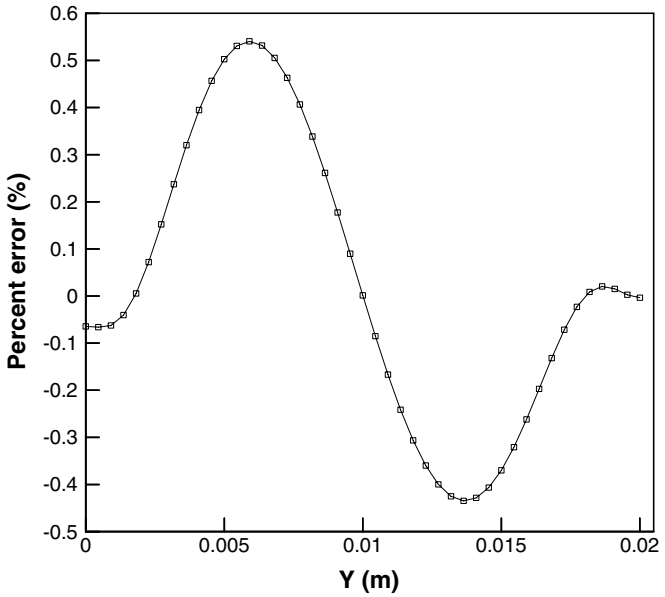

Fig. 19. Percent errors of the solid–liquid distance at $t = 0.6$ for the sequential method for the case 1.

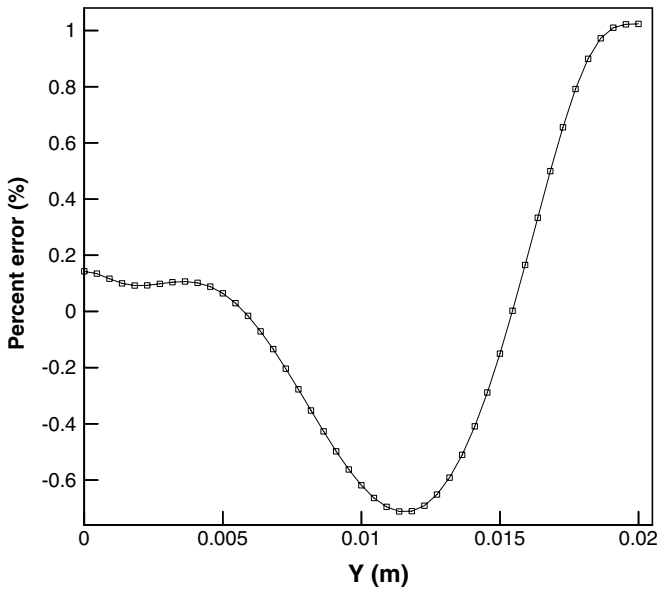

Fig. 20. Percent errors of the solid–liquid distance at $t = 0.6$ for the whole time-domain method for the case 2.

the L-curve plots are also taken, and the optimal regularization parameters are chosen in the same manner.

3.3.5. Optimal heat flux solutions

Using the optimal regularization parameter found in the L-curve method, the optimal heat flux solutions are found for the cases 1 and 2 in both the sequential method and the whole time-domain method with the piecewise polynomial function. Fig. 16a and b show the optimal heat flux solutions in case 1 for the sequential method and the whole time-domain method. These heat flux solutions are almost identical. Fig. 17a and b show the optimal heat flux solution for the sequential method in the case 2. We also find that the heat flux solution for the whole time-domain method is almost identical to the heat flux solution for the sequential method. Since we divide the time domain for the heat flux solution into three parts, non-smooth functions with kinks for the heat flux distribution are seen at the boundaries of the time domains ($t = 0.2$ s, 0.4 s).

3.3.6. Validation of the inverse design solutions and comparison of the sequential method and the whole time-domain method

Fig. 18a and b show time history of the standard deviation σ Eq. (37) for the error of the solid–liquid distance in the cases 1 and 2, respectively. The standard deviation in

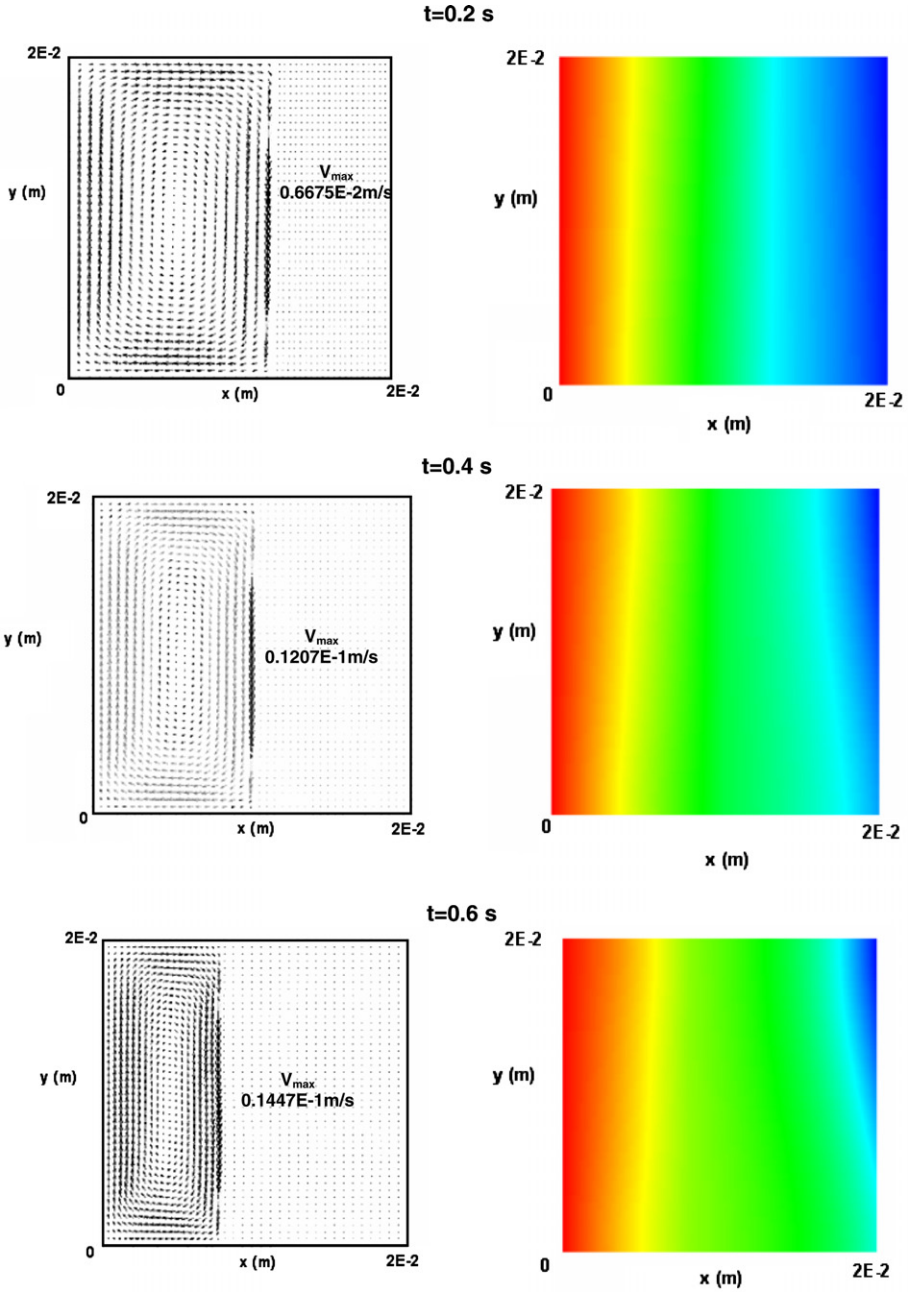

Fig. 21. Velocity (left) and temperature (right) distributions at times $t = 0.2, 0.4, 0.6$ for the case 1.

the earlier time stage of each time domain ($t = 0.2, 0.4$ s) is found to be less accurate in the sequential method. This is because the heat flux on the right wall diffuses toward the solid–liquid interface, and the diffusion time is required for a thermal front to penetrate the solid domain and reach the solid–liquid interface. Thus, it is physically difficult to control the solid–liquid interface immediately after the initial time. The error of the whole time-domain method with the piecewise polynomial functions is more damped and slightly accurate than that of the sequential method. Overall, the standard deviations for the error of distance in both the sequential and whole time-domain methods are small enough to consider that our inverse algorithm is reasonably accurate to control the solid–liquid distance. Fig. 19 shows percent errors of the solid–liquid distance at $t = 0.6$ for the sequential method for case 1. The percent errors of the sequential method are ten times smaller than in the whole time-domain with nine unknowns (Fig. 11). Fig. 20 shows percent errors of the solidification distance at $t = 0.6$ for the whole time-domain method for the case 2. The percent errors are less than 1%. Figs. 21 and 22 show the velocity and temperature distributions at $t = 0.2, 0.4, 0.6$ in the cases 1 and 2 for the sequential method by using the optimal heat flux distributions. The cold temperature distributions are seen at the upper right corner to eliminate the effect of natural convection. We also see that the solid–liquid interface moves leftward at a constant velocity as we specified in our calculation.

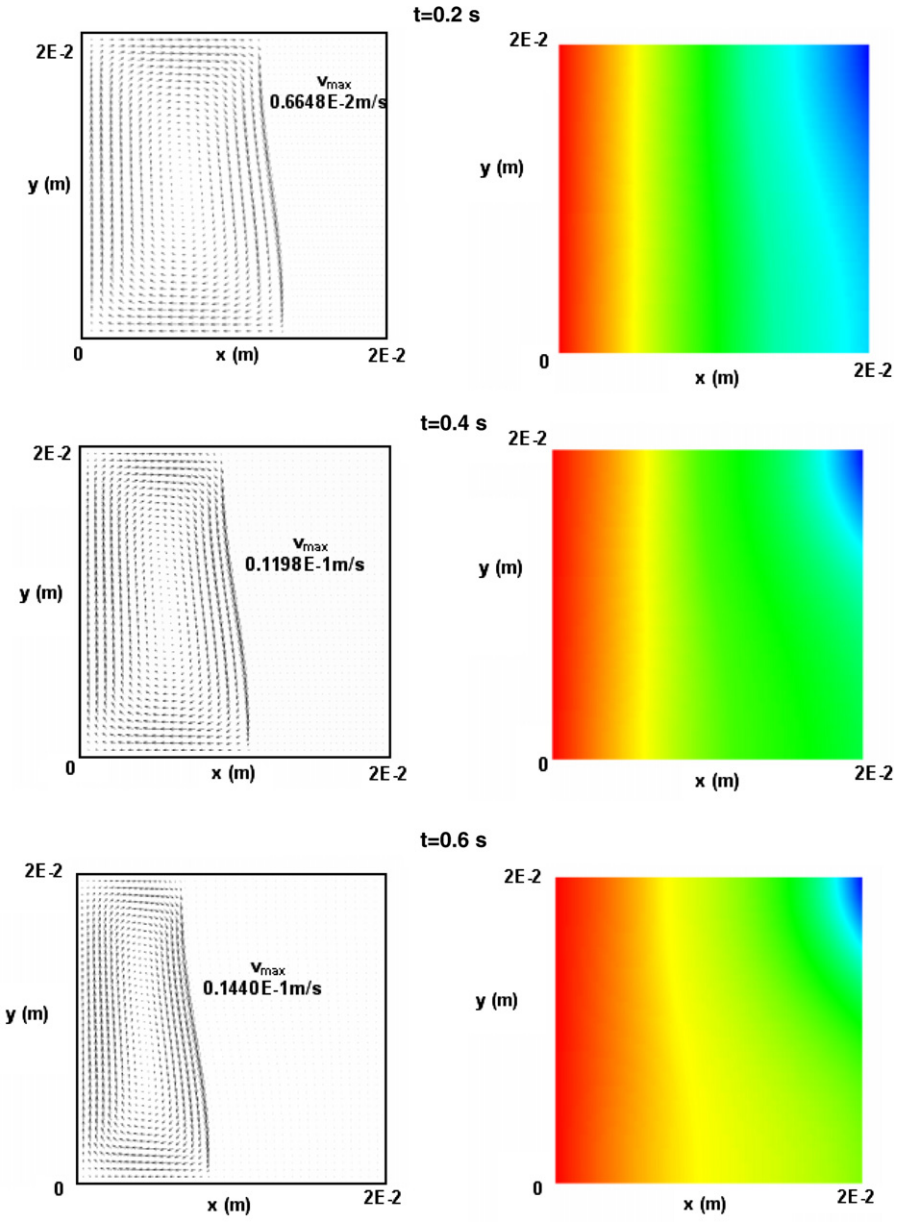

Fig. 22. Velocity (left) and temperature (right) distributions at times $t = 0.2, 0.4, 0.6$ for the case 2.

4. Concluding remarks

This paper has presented a computational algorithm for the inverse design of solidification processing systems. The algorithm entails the use of the Tikhonov regularization method, along with an appropriately selected regularization parameter. The direct solution of the moving boundary problem is solved using the deforming finite element method. The direct and inverse formulations are presented. The determination of the optimal regularization parameter α using the L-curve method is also given. The design algorithm is applied to determine the appropriate boundary heat flux distribution to obtain prescribed solid–liquid interface in a 2-D cavity. The whole time-domain method and the sequential method are used to approximate the optimal heat flux solutions. These results show that the sequential method is comparative to the whole time-domain method if the diffusion time of the heat flux is cautiously considered. We also find that the regularization method with L-curve is reasonably accurate for designing solidification processing systems.

Acknowledgement

The authors gratefully acknowledge the financial support of NASA (Grant #: NAG8-1697).

References

[1] K. Okamoto, B.Q. Li, Optimal regularization methods for inverse heat transfer problems, in: ASME Summer Heat Transfer Conference, Charlotte, NC, CD ROM, July 2004.
[2] M. Krishnan, D.G.R. Sharma, Determination of the interfacial heat transfer coefficient in unidirectional heat flow by Beck's nonlinear estimation procedure, Int. Commun. Heat Mass Transfer 23 (2) (1996) 203–214.
[3] D. O'Mahoney, D.J. Browne, Use of experiment and an inverse method to study interface heat transfer during solidification in the investment casting process, Exp. Thermal Fluid Sci. 22 (2000) 111–122.
[4] R. Xu, G.F. Naterer, Inverse method with heat and entropy transport in solidification processing of materials, J. Mater. Process. Tech. 112 (2001) 98–108.
[5] S. Hale, M. Keyhani, J.I. Frankel, Design and control of interfacial temperature gradients in solidification, Int. J. Heat Mass Transfer 43 (2000) 3795–3810.
[6] G.S. Dulikrabich, M.J. Colaco, T.J. Martin, S. Lee, An inverse method allowing user-specified layouts of magnetized microfibers in solidifying composites, J. Composite Mater. 37 (2003) 1351–1365.
[7] N. Zabaras, T.H. Nguyen, Control of the freezing interface morphology in solidification process in the presence of natural convection, Int. J. Numer. Meth. Engng. 38 (1995) 1555–1578.
[8] N. Zabaras, Inverse finite element techniques for the analysis of solidification process, Int. J. Numer. Meth. Engng. 29 (1990) 1569–1587.
[9] S. Kang, N. Zabaras, Control of the freezing interface motion in two-dimensional solidification processes using the adjoint method, Int. J. Numer. Meth. Engng. 38 (1995) 63–80.
[10] N. Zabaras, S. Kang, On the solution of an ill-posed design solidification problem using minimization techniques in finite and infinite-dimensional function spaces, Int. J. Numer. Meth. Engng. 36 (1993) 3973–3990.
[11] G.Z. Yang, N. Zabaras, An adjoint method for the inverse design of solidification processes with natural convection, Int. J. Numer. Meth. Engng. 42 (1998) 1121–1144.
[12] K. Okamoto, B.Q. Li, Inverse design of solidification processes, ASME International Mechanical Engineering Congress and RD&D Expo Anaheim, CA, CD ROM, November 2004.
[13] Y. Shu, B.Q. Li, H.C. de Groh, Magnetic damping of g-jitter induced double diffusive convection in microgravity, Numer. Heat Transfer 42 (4) (2002) 345–364.
[14] K. Li, B.Q. Li, H.C. de Groh, Numerical analysis of double-diffusive convection/solidification under g-jitter/magnetic fields, J. Thermophys. Heat Transfer 17 (2) (2003) 199–209.
[15] S.P. Song, B.Q. Li, A hybrid boundary/finite element method for simulating viscous flows and shapes of droplets in electric fields, Int. J. Comput. Fluid Dyn. 15 (1) (2002) 125–144.
[16] Y. Shu, An experimental and numerical study of natural convection and solidification in constant and oscillating temperature fields, Ph.D. thesis, Washington State University Pullman, WA, 2003.
[17] P.C. Hansen, D.P. O'leary, The use of the L-curve in the regularization of discrete ill-posed problems, SIAM J. Sci. Comput. 14 (1993) 1487–1503.